

Comparison of symbolic regression algorithms in Star/galaxy/quasar separation

Rachit Deshpande^a, Shantanu Desai^b

^aDepartment of Artificial Intelligence, IIT Hyderabad, Kandi, Telangana-502284, India

^bDepartment of Physics, IIT Hyderabad, Kandi, Telangana-502284, India

Abstract

This work investigates symbolic regression (SR) as an interpretable alternative to black-box machine learning for the classification of stars, galaxies, and quasars in the Sloan Digital Sky Survey Data Release 17 (SDSS DR17). We conduct a systematic comparative study of four state-of-the-art SR frameworks: PySR , Exhaustive Symbolic Regression (ESR) with MDL-based selection, Physical Symbolic Optimization (PhySO) using deep reinforcement learning, and Multi-View Symbolic Regression (MvSR). By deriving compact analytic functions (complexity ≤ 10) on a representative training subset and subsequently evaluating them via a 5-fold stratified cross-validation protocol on 100,000 spectroscopically confirmed objects, we map spectroscopic redshift (z) to continuous classification scores. Our results demonstrate that these low-complexity expressions achieve high predictive reliability, with MvSR reaching a Cohen's Kappa of 0.8948 and PhySO achieving exceptional parametric stability ($\sigma < 0.002$). We show that these models not only match the performance of traditional baselines but also provide a transparent, mathematically concise characterization of the astrophysical boundaries separating Galactic and extragalactic populations.

Keywords: Symbolic Regression, Astroinformatics, Spectroscopic Classification, Star-Galaxy-Quasar Separation, Deep Reinforcement Learning, Explainable AI (XAI), Genetic Programming, Information Theory, Interpretable Machine Learning, Scientific Machine Learning (SciML), SDSS DR17.

1. INTRODUCTION

Photometric classification of stars, galaxies, and quasars from large-scale astronomical surveys underpins a wide range of analyses in cosmology, galaxy evolution, and active galactic nuclei studies (Soumagnac et al., 2015). A large number of machine learning approaches, particularly deep neural networks and gradient-boosted trees have been applied to the problem of object classification using data from photometric surveys such as Blanco Cosmology Survey, Sloan Digital Sky Survey (SDSS), Dark Energy Survey etc (Desai et al., 2012; Sevilla-Noarbe et al., 2018; Chaini et al., 2023; Bhavanam et al., 2024; Slater et al., 2020; Logan and Fotopoulou, 2020) (and references therein). Some of these achieve classification accuracies exceeding 95% (Solorio-Ramírez et al., 2023) on SDSS DR17 (Abdurro'uf et al., 2022). However, these “black box” models obscure the underlying astrophysical relationships—such as redshift evolution and population density gradients—that govern object separability (Hassija et al., 2024).

To ameliorate this problem, symbolic regression (SR) provides a compelling alternative by jointly optimizing predictive performance and mathematical interpretability (Bartlett et al., 2025; Desmond, 2025). Rather than learning opaque weight matrices, SR searches directly for analytic expressions that map input features to continuous class scores. These scores can subsequently be thresholded into discrete labels, providing a

transparent decision manifold. Recent advances have produced a diverse set of SR methodologies: stochastic genetic programming (PySR) (Cranmer, 2023), deterministic exhaustive enumeration (ESR) (Bartlett et al., 2022), reinforcement learning-guided methods with unit constraints (PhySO) (Tenachi et al., 2023), and ensemble-style strategies like Multi-View Symbolic Regression (MvSR) (Russeil et al., 2024). These have recently been applied to a variety of problems in Astrophysics and Cosmology (See Patra et al. 2026; Darc et al. 2025; Martín et al. 2026; Sousa-Neto et al. 2025 for a non-exhaustive list of recent applications of symbolic regression).

About a year ago, Llorella and Cebrian (2025) applied the PySR symbolic regression algorithm to SDSS DR17 data to derive an analytical expression which was used to separate stars, galaxies, and quasars. A genetic algorithm was also used to optimize the hyperparameters. The resulting combination achieved a Cohen Kappa value of 0.81. We extend the analysis in Llorella and Cebrian (2025) and consider four complementary SR approaches to the same problem of star/galaxy/quasar classification on the same SDSS DR17 data, under a unified, 5-fold stratified cross-validation protocol. By restricting the input space to the spectroscopic redshift (z), we isolate and evaluate the capacity of each method to discover compact redshift-centric decision functions. Our analysis focuses not only on classification metrics such as Cohen's Kappa and Balanced Accuracy—where we achieve results exceeding 0.89 and 92%, respectively—but also on the parametric stability of the optimized decision thresholds (t_1 and t_2). This comprehensive evaluation provides a rigorous assessment of the utility of symbolic regression as a transparent

Email addresses: ai24mtech11003@iith.ac.in (Rachit Deshpande), shantanud@phy.iith.ac.in (Shantanu Desai)

Class distribution in SDSS DR17 sample

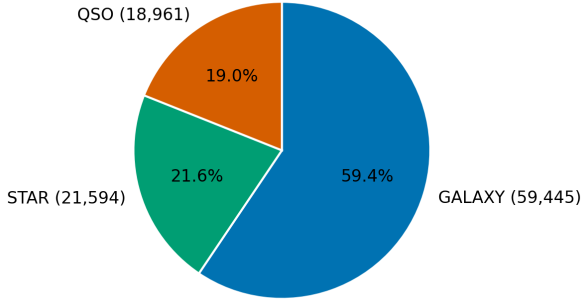


Figure 1: Class distribution of the SDSS DR17 dataset across GALAXY, STAR, and QSO categories.

and reliable tool for automated astronomical discovery.

This manuscript is structured as follows. The dataset is described in Sect. 2. The methodology is described in Sect. 3, results in Sect. 4, and we conclude in Sect. 5.

2. Dataset

We analyze the stellar classification catalog from SDSS DR17, which contains 100,000 spectroscopically confirmed objects labeled as galaxies, stars, or quasars. After removing the entries with missing redshift or class values and standardizing labels (mapping “QUASAR” to “QSO”), the final working sample consists of 59,445 galaxies (59.45%), 21,594 stars (21.59%), and 18,961 quasars (18.96%).

Figure 1 illustrates the pronounced class imbalance in the dataset, with galaxies forming the clear majority. Such imbalance presents well-known challenges for machine learning classifiers (Bethapudi and Desai, 2018), particularly when evaluating performance on the underrepresented QSO population. For the symbolic discovery phase, a representative 10% subset (10,000 objects) of the dataset was utilized (similar to Llorella and Cebrian (2025)) to ensure computational efficiency while preserving population diversity and class proportions. The discovered equations were subsequently validated against the entire 100,000-object dataset using 5-fold cross-validation.

The redshift distributions shown in Figure 2, presented as normalized histograms with a logarithmic y-axis, exhibit characteristic population signatures that strongly motivate redshift-only classification. Stars concentrate in a narrow peak at $z \approx 0$, corresponding primarily to Galactic foreground objects. Galaxies form a broad distribution peaking between $z \sim 0.1$ and $z \sim 0.8$, typical of luminous red galaxies in this spectroscopic sample. Quasars display an extended high-redshift tail beyond $z \sim 2$, reaching values exceeding $z > 6$.

Figure 3 shows the $u - g$ color–redshift relation, revealing systematic population differences. Stars follow the well-known stellar locus with minimal redshift evolution, while galaxies occupy a relatively stable intermediate-color region across the observed range (Desai et al., 2012). Quasars, however, exhibit

Redshift distributions by class

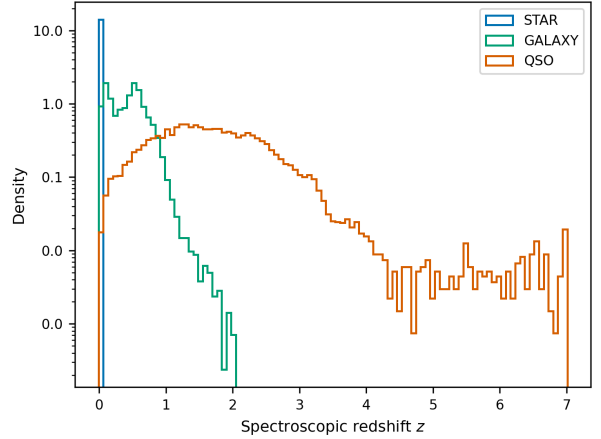


Figure 2: Normalized redshift distributions of stars, galaxies, and quasars shown on a logarithmic scale.

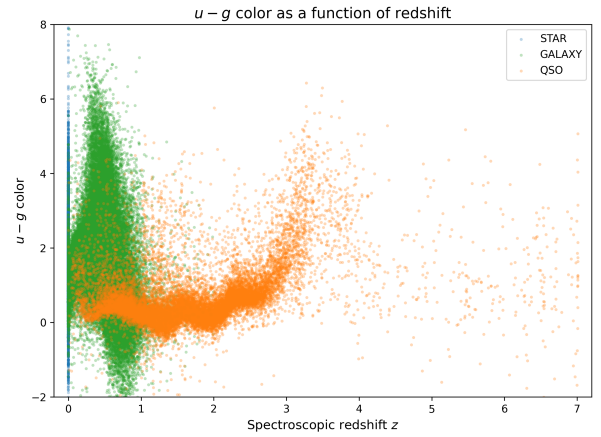


Figure 3: $u - g$ color as a function of redshift for stars, galaxies, and quasars, highlighting population-specific trends.

pronounced color evolution; they typically appear blue (exhibiting a UV-excess with $u - g \lesssim 1$) at low redshifts, but transition to significantly redder colors ($u - g \gtrsim 2$) at $z > 2.5$ as Lyman- α forest absorption enters the SDSS u -band (Richards et al., 2002).

These empirical distributions provide strong motivation for developing compact symbolic regression models using redshift alone. The three populations occupy systematically distinct regions of this one-dimensional parameter space, suggesting that simple, mathematically concise analytic functions $f(z)$ can achieve meaningful class separation without the need for high-dimensional color spaces.

3. Methodology

3.1. General Approach

Our methodology seeks to construct interpretable decision functions that map spectroscopic redshift to astrophysical class membership. Specifically, we learn continuous score functions $s(z)$ that take the redshift z as input and produce a scalar score

predictive of the underlying object class. Two optimized thresholds, t_1 and t_2 (where $t_1 < t_2$), are used to convert the continuous score into discrete class labels. This process follows the decision manifold described in Eq. 1.

$$\text{Class}(z) = \begin{cases} \text{GALAXY} & \text{if } s(z) < t_1 \\ \text{STAR} & \text{if } t_1 \leq s(z) \leq t_2 \\ \text{QSO} & \text{if } s(z) > t_2 \end{cases} \quad (1)$$

This formulation allows each symbolic regression method to express class separation through a compact analytic function, while preserving a transparent and physically interpretable decision structure. Unlike traditional black-box classifiers that rely on high-dimensional softmax layers, this one-dimensional scoring manifold forces the frameworks to discover the natural ordering of astrophysical populations along the redshift axis—beginning with nearby Galactic stars at $z \approx 0$ and extending to high-redshift quasars at $z > 2$.

By restricting the input to a single physically meaningful parameter, we isolate the representational capacity of each symbolic framework and evaluate its ability to capture the non-linear boundaries between populations using mathematically concise expressions.

3.2. Experimental Protocol and Data Preprocessing

The SDSS DR17 sample used in this study consists of 100,000 spectroscopically confirmed objects after standardizing class labels (mapping “QUASAR” to “QSO”) (Abdurro’uf et al., 2022). The final class distribution is GALAXY (59.45%), STAR (21.59%), and QSO (18.96%). No entries with missing redshift or class labels were present in the cleaned dataset.

To maintain computational efficiency during the symbolic discovery phase—particularly for exhaustive symbolic regression (ESR) and genetic search frameworks such as PySR and MvSR—a representative 10% subset (10,000 objects) is initially sampled from the entire dataset, similar to that done in Llorella and Cebrian (2025). This static subset enables deep exploration of the functional search space, while preserving the underlying astrophysical population density and class balance, allowing the models to discover a universal scoring function $s(z)$.

Once the scoring functions are determined, we adopt a five-fold stratified cross-validation protocol on the full 100,000-object dataset to ensure statistical robustness. In each fold, approximately 80% of the data (80,000 samples) is used for threshold calibration and 20% (20,000 samples) for testing

A critical component of our unified protocol is the automated grid-search algorithm used to calibrate the decision thresholds t_1 and t_2 . For every discovered scoring function $s(z)$, the algorithm searches candidate threshold pairs within the range defined by the 5th and 95th percentiles of the training fold scores. The pair (t_1, t_2) that maximizes Cohen’s κ coefficient (cf. Eq. 24) is selected and subsequently evaluated on the unseen test set.

This procedure ensures that classification boundaries are optimally tuned for each symbolic framework under identical conditions, providing a fair benchmark of their respective mathematical search strategies. The final performance metrics are

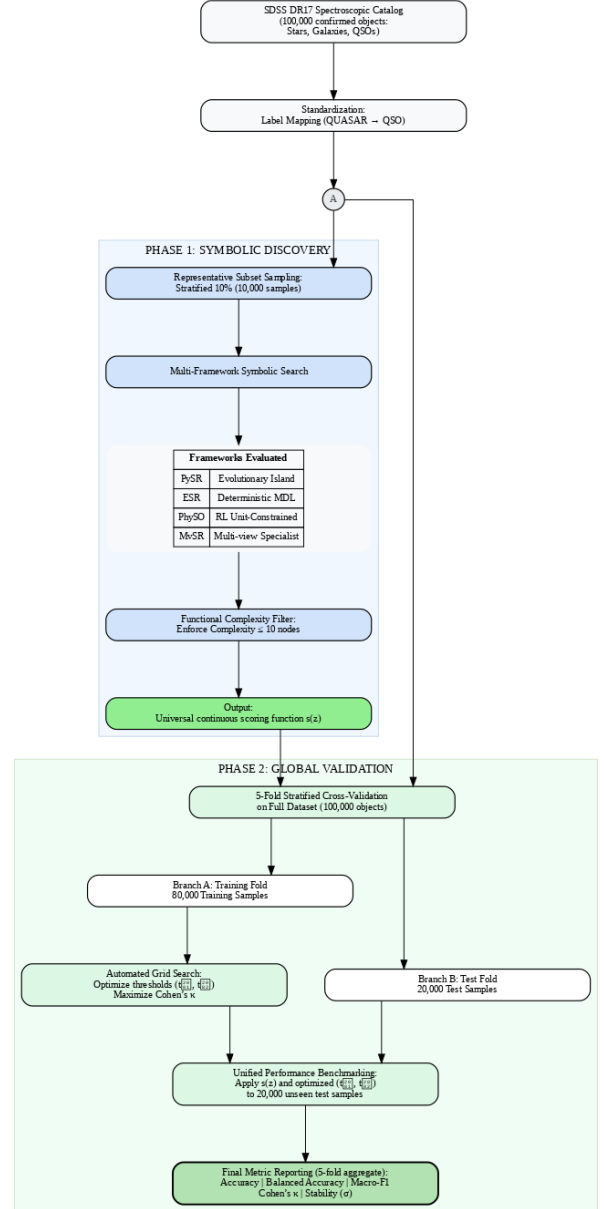


Figure 4: Unified experimental pipeline for SDSS DR17 classification.

reported as mean values with standard deviations in all the five stratified folds. The complete end-to-end pipeline, from symbolic discovery on the representative subset to global validation via stratified cross-validation on the full dataset, is summarized in Figure 4.

3.3. Symbolic Regression Algorithms

Symbolic regression (SR) simultaneously discovers both the mathematical structure and numerical parameters of analytic expressions, offering a transparent alternative to traditional fixed-form regression. By representing candidate expressions as tree structures, SR navigates an expansive functional space to identify the most parsimonious mapping between input features and target scores.

In the context of SDSS DR17, this approach allows for the discovery of explicit decision functions, $s(z)$, that encode the astrophysical boundaries separating Galactic stars, galaxies, and high-redshift quasars. As detailed in Section 3.2, each of the following four frameworks is evaluated under an identical five-fold stratified protocol, with decision thresholds (t_1, t_2) optimized to maximize the Cohen’s κ coefficient. This ensures that the comparison isolates each framework’s intrinsic ability to capture the non-linear transition regions of the one-dimensional redshift manifold. We now discuss the different symbolic regression algorithms used in this work. A comparative overview of the engines, optimization objectives, and inductive biases for these four symbolic frameworks is provided in Table 1.

3.3.1. PySR: Evolutionary Island-Model Search

We employ PySR, a high-performance symbolic regression framework based on an island-model evolutionary algorithm. In this architecture, multiple semi-independent subpopulations (“islands”) evolve in parallel, with periodic migration of candidate expressions between islands. This strategy mitigates premature convergence and promotes structural diversity within the evolving symbolic population.

Search Configuration and Operator Set. The functional search space is defined by the binary operator set as follows:

$$\mathcal{O}_{\text{binary}} = \{+, -, \times, \div\}, \quad (2)$$

and the unary operator set below:

$$\mathcal{O}_{\text{unary}} = \{\text{exp}\}. \quad (3)$$

To ensure numerical stability and physical consistency, protected operator variants are used for division, and nested exponential constraints are imposed to prevent unstable recursive growth. To prioritize interpretability and parsimony, the symbolic complexity is strictly bounded as shown below:

$$\text{Complexity}(s) \leq 10, \quad (4)$$

where complexity is measured as the total number of nodes in the expression tree. The search objective minimizes the regularized L^2 loss, defined as follows:

$$\mathcal{L}_{\text{SR}} = \frac{1}{N} \sum_{i=1}^N (s(z_i) - y_i)^2, \quad (5)$$

where $s(z)$ is the candidate symbolic function and y_i denotes the target encoding, and N represents the number of training samples. The evolutionary process is executed for 500 iterations in a representative 10,000-sample subset. This subset is partitioned into 5,000 training samples for functional evolution and 5,000 validation samples used for the selection of fitness-based models. The process is accelerated through Julia-based multi-threading, enabling evaluation of thousands of candidate expressions per second.

Evolutionary Strategy and Refinement. The evolutionary process employs tournament selection combined with structural genetic operators, including subtree crossover, point mutation, and elitist reproduction. Algebraic simplification rules—specifically constant folding and identity elimination—are iteratively applied to maintain compact functional forms.

After structural discovery, numerical constants are refined via local BFGS optimization:

$$\theta^* = \arg \min_{\theta} \mathcal{L}_{\text{SR}}(s_{\theta}), \quad (6)$$

where θ represents the continuous parameters embedded in the symbolic structure. This refinement improves numerical precision without modifying the discovered analytic form.

Model Selection and Thresholding. Although the internal search is guided by complexity-regularized L_2 loss, the final universal scoring function $s(z)$ is selected using a custom multi-objective validation metric. While the initial search space is mapped via the Pareto-optimal trade-off between functional complexity and L_2 loss (visualized in Figure 5), the final representative scoring function is extracted from this frontier by ranking candidate expressions according to:

$$\text{Score} = 0.4 \cdot \text{Accuracy} + 0.4 \cdot \kappa - 0.2 \cdot \frac{\text{Complexity}}{10}. \quad (7)$$

This selection protocol balances predictive performance, class agreement (Cohen’s κ), and structural parsimony.

Following the unified evaluation protocol described in Section 3.2, the continuous outputs of $s(z)$ are converted into discrete class labels by calibrating decision thresholds t_1 and t_2 on the validation set:

$$(t_1, t_2) = \arg \max_{t_1 < t_2} \kappa_{\text{val}}. \quad (8)$$

This ensures that the final analytic expression achieves optimal class separation across astrophysical populations while remaining mathematically concise and interpretable.

3.3.2. Exhaustive Symbolic Regression (ESR) with MDL Selection

To provide a deterministic baseline free from the stochastic variability inherent in evolutionary search, we implement Exhaustive Symbolic Regression (ESR). Unlike heuristic methods, ESR guarantees the evaluation of the complete mathematically valid candidate set within a predefined complexity limit, enabling principled and reproducible model selection.

Search Space and Structural Filtering. The candidate expressions are constructed from a basis library of binary operators

$$\mathcal{O}_{\text{binary}} = \{+, -, \times, \div\}, \quad (9)$$

and the unary operator

$$\mathcal{O}_{\text{unary}} = \{\text{exp}\}. \quad (10)$$

The terminal nodes consist of the spectroscopic redshift z and learnable scalar constants c_n . To maintain computational

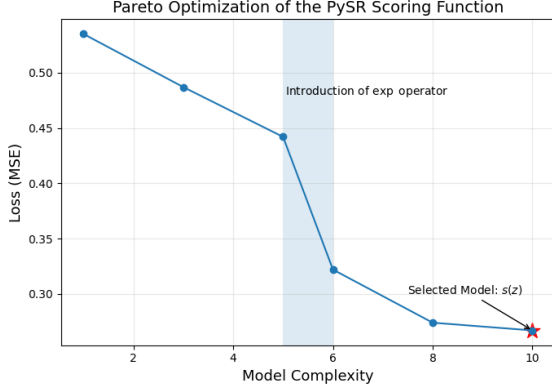


Figure 5: Pareto-optimal frontier for the `PySR` discovery phase. The plot illustrates the trade-off between functional complexity and L_2 loss. A significant performance gain is observed at $C = 6$, corresponding to the introduction of the exponential (`exp`) operator, which captures the non-linear population transitions. The final scoring function $s(z)$ (indicated by the star) was selected at the complexity limit of $C = 10$ to maximize representational accuracy while maintaining interpretability, following the scaling law selection criteria discussed in [Darc et al. \(2025\)](#).

tractability while ensuring deep functional exploration, we enforce a strict complexity bound

$$C(s) \leq 10. \quad (11)$$

To ensure astrophysical relevance and numerical stability, the framework applies three specific structural filters during the enumeration process:

Redshift Requirement: Expressions lacking the input variable z are discarded to ensure the scoring function is dependent on the primary physical feature.

Nested Exponential Filter: Recursive exponential forms (e.g., $\exp(\exp(z))$) are prohibited to prevent mathematical instability and unphysical growth.

Functional Constraints: Exponential terms are restricted to valid physical forms, specifically targeting motifs like $\exp(c \cdot z)$, which characterize redshift-based density transitions.

Parameter Optimization. For expressions containing free constants, we employ an `L-BFGS` optimization strategy to minimize the Mean Squared Error (MSE) ([Liu and Nocedal, 1989](#)). To ensure global convergence and prevent entrapment in local minima, the optimizer is initialized through a multi-start parallel routine. This process executes 30 independent optimizations per expression from randomized initial positions within a broad parameter space.

Information-Theoretic Model Selection (MDL). Model selection is governed by the Minimum Description Length (MDL) principle. To ensure computational tractability during the exhaustive search, we implement the Bayesian Information Criterion (BIC) formulation ([Krishak and Desai, 2020](#)) of the MDL score, which [Bartlett et al. \(2022\)](#) note can be derived as a special case of the exact description length. The MDL framework identifies the optimal model by balancing predictive fidelity against structural and parametric complexity. This information-theoretic competition is visualized in [Figure 6](#), where the final model is identified

at the global minimum of the total description length. The MDL score for an expression s is calculated as follows:

$$S_{\text{MDL}} = \mathcal{L}_{\text{neg}} + C(s) \ln(N_{\text{ops}} + 1) + \frac{k}{2} \ln(N). \quad (12)$$

where, \mathcal{L}_{neg} denotes the negative log-likelihood, which can be calculated as follows:

$$\mathcal{L}_{\text{neg}} = 0.5 N \ln(2\pi \cdot \text{MSE}) + 0.5 N. \quad (13)$$

The other terms in [Eq. 12](#) are defined as follows:

- $C(s) \ln(N_{\text{ops}} + 1)$: The structural complexity penalty based on the operator library size N_{ops} .
- $\frac{k}{2} \ln(N)$: The penalty parameter for the k optimized constants across N data points.

Evaluation Protocol. Following the unified protocol established in [Section 3.2](#), the top-ranked `ESR` model per fold is used to generate continuous scores $s(z)$. Decision thresholds t_1 and t_2 are then calibrated on the validation split via grid search to maximize the Cohen’s κ coefficient, ensuring a rigorous benchmark against the evolutionary and reinforcement learning-based frameworks.

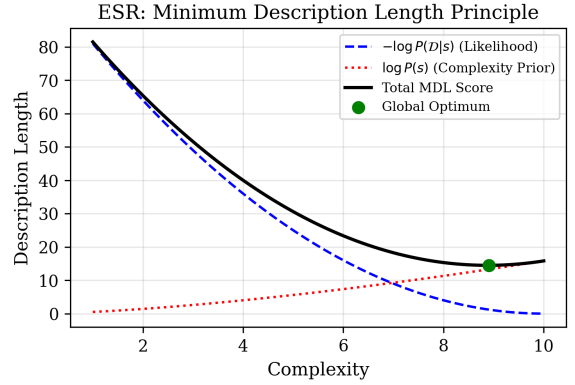


Figure 6: Model selection in `ESR` via the Minimum Description Length (MDL) principle. The plot illustrates the information-theoretic competition between the negative log-likelihood (goodness of fit, [Eq. 13](#)) and the complexity prior (parsimony penalty, [Eq. 12](#)). The final model is selected at the global minimum of the total description length (indicated by the green dot), ensuring the discovery of a non-overfitted, physically parsimonious scoring function as established in [Bartlett et al. \(2022\)](#)

3.3.3. Deep Reinforcement Learning Symbolic Regression (PhySO)

We implement a reinforcement learning-based symbolic regression framework inspired by the Physical Symbolic Optimization (`PhySO`) architecture. This method reformulates symbolic discovery as a sequential decision-making process, utilizing a deep neural network to navigate the functional search space while maintaining mathematical consistency.

Expression Generation as a Sequential Process. Symbolic expressions are generated in prefix notation using an autoregressive Long Short-Term Memory (LSTM) network. At each discrete time step t , the policy π_θ samples a token a_t from a predefined vocabulary V :

$$V_{\text{op}} = \{+, -, \times, \div\}, \quad V_{\text{exp}} = \{\text{exp}\}, \quad V_{\text{term}} = \{z, c\}. \quad (14)$$

In Eq. 14, z represents the spectroscopic redshift and c denotes learnable scalar constants. The construction is formulated as a Markov Decision Process (MDP), where the RNN controller generates sequences up to a maximum length of 10 nodes, ensuring parsimonious mathematical structures.

Structural Constraints and Filtering. To ensure the discovery of stable and physically plausible analytic forms, the framework applies a multi-layered filtering mechanism during the sampling process. As conceptually illustrated in Figure 7, the reinforcement learning agent employs a masking function to prune mathematically or physically invalid paths in real-time:

Redshift Requirement: The generated expressions must contain the input variable z to ensure functional dependence on the primary astrophysical feature.

Nested Exponential Filter: Recursive exponential forms (e.g., $\text{exp}(\text{exp}(z))$) are strictly prohibited to prevent mathematical instability and unphysical growth.

Prefix Validity: Sampled sequences are verified against operator parity rules; only mathematically sound expression trees are permitted for reward evaluation.

By aggressively masking out mathematically or physically invalid paths, the neural network concentrates its search entirely within the space of consistent analytic forms.

Policy Optimization and Reward Mechanism. The policy parameters θ are optimized using a risk-seeking policy gradient strategy. Unlike standard reinforcement learning that maximizes mean performance, this approach emphasizes the top-performing fraction of sampled expressions—defined by a 90th percentile threshold—to encourage exploration of high-reward regions. The agent is trained using the Adam optimizer with a learning rate of 0.0025 and a softmax temperature of 1.15 to balance exploration and exploitation. The reward $R(s)$ for a generated expression $s(z)$ is derived from its predictive fidelity relative to the target ordinal labels y . This reward is bounded between (0, 1] and is calculated as:

$$R(s) = \frac{1}{1 + \text{MSE}(s(z), y)}. \quad (15)$$

The search is conducted on the initial 10,000-sample representative subset. It utilizes a batch size of 3,000 expressions per iteration over 200 generations, employing an exponential moving average (EMA) baseline with $\beta = 0.95$ to stabilize policy updates.

Numerical Parameter Refinement. For expressions containing free constants c_n , we utilize a high-performance L-BFGS optimizer with a history size of 20 and Strong-Wolfe line search to refine numerical parameters. To maintain stability, our implementation utilizes protected operator variants, including clamped exponentials ($\text{exp}(x)$ limited to ± 12.0) and safe division (clamped at $\epsilon = 10^{-6}$), ensuring well-behaved gradients during optimization.

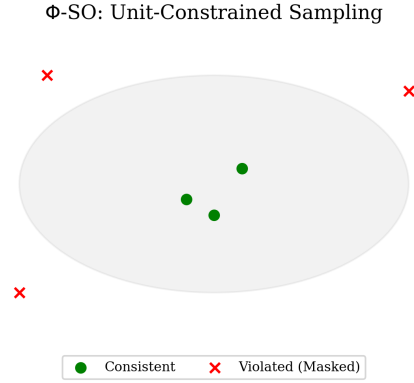


Figure 7: Unit-constrained sampling in Φ -SO. The reinforcement learning agent utilizes a masking function to eliminate candidate tokens that would violate mathematical or structural consistency (red crosses). By restricting sampling to a valid functional manifold (shaded region), the framework efficiently identifies stable and physically plausible scoring motifs (green circles), as described in Tenachi et al. (2023).

3.3.4. Multi-View Symbolic Regression (MvSR)

Multi-view symbolic regression addresses the non-stationarity of the SDSS redshift distribution by decomposing the discovery task into distinct functional regimes. This approach allows the framework to specialize in localized astrophysical structures while maintaining a globally consistent analytic template.

The input domain is partitioned into three disjoint, contiguous views representing dominant object populations:

- **View 1:** Low-redshift (primarily stellar-dominated).
- **View 2:** Intermediate-redshift (galaxy-dominated).
- **View 3:** High-redshift (quasar-dominated).

The decomposition of the input domain into these specialized regimes is visualized in Figure 8. In our implementation, the dataset is divided into three equal-sized contiguous segments to ensure each specialized view contains a representative population density. Within each view, the data is further partitioned into 50% training and 50% validation samples to facilitate localized parameter refinement and objective assessment.

Independent Evolution and Aggregated Fitness. The search utilizes a genetic programming population of 1,000 individuals evolved over 35 generations with a basis library of

$$O_{\text{binary}} = \{+, -, \times, \div\}, \quad O_{\text{unary}} = \{\text{exp}\}. \quad (16)$$

Unlike single-view methods, the fitness of a candidate expression $s(z)$ is determined by its Aggregated MSE, defined as the maximum error observed across all three views:

$$L_{\text{agg}} = \max(\text{MSE}_{\text{View1}}, \text{MSE}_{\text{View2}}, \text{MSE}_{\text{View3}}). \quad (17)$$

This ‘‘min-max’’ objective ensures that the discovered functional form is robust across the entire redshift manifold and prevents the majority galaxy population from dominating the mathematical search.

View-Specific Parameter Refinement. While the symbolic structure (e.g., $s(z) = c_1 + c_2/(z + \exp(c_3z))$) is globally shared, its numerical constants (c_n) are refined independently for each view. For every candidate expression, a GPU-accelerated L-BFGS optimizer is used to find the optimal parameters ($\theta_1, \theta_2, \theta_3$) that minimize the MSE within each respective redshift regime. This allows the template to adapt its coefficients to the specific physical density gradients of different astrophysical populations.

Following the unified protocol established in Section 3.2, the continuous scores generated by the best-performing multi-view model are used to calibrate decision thresholds t_1 and t_2 . These thresholds are optimized on the validation split via grid search to maximize the Cohen’s κ coefficient, ensuring a rigorous benchmark against both single-view and exhaustive methods.

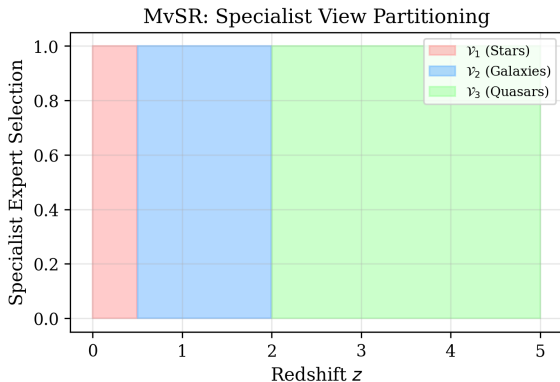


Figure 8: Specialist view partitioning in $MvSR$. The redshift domain is decomposed into three contiguous, non-overlapping regimes: \mathcal{V}_1 (Stars), \mathcal{V}_2 (Galaxies), and \mathcal{V}_3 (Quasars). This partitioning is implemented by dividing the dataset into three equal-sized segments, ensuring each specialist population has sufficient training density. This multi-view decomposition enables the framework to adapt a single global symbolic template to localized astrophysical structures by evolving independent numerical parameters for each regime, following the parametric multi-dataset integration logic in [Russeil et al. \(2024\)](#).

3.4. Machine Learning Benchmarks

To establish a formal performance ceiling for the one-dimensional redshift manifold, we implement three distinct machine learning paradigms, following the theoretical foundations of pattern recognition and the connectionist framework established in [Bishop \(2006\)](#). The inclusion of these high-capacity benchmarks—specifically Random Forests, SVMs, and MLPs—is essential to define the Information-Theoretic Ceiling of the spectroscopic redshift distribution. As noted by [Cranmer](#)

(2023), symbolic regression is an NP-hard optimization problem where the functional search space is uncountably infinite. Therefore, we utilize these non-interpretable paradigms to establish a definitive performance upper bound. These models serve as a control group to quantify the trade-off between black-box accuracy and symbolic transparency, allowing us to determine if the discovered expressions are physically sufficient or if they suffer from a ‘‘complexity deficit’’ compared to overparameterized architectures. All models are restricted to the feature space $X = \{z\}$ to ensure a direct comparative basis with the symbolic frameworks. The paradigms, optimization strategies, and underlying inductive biases for these non-interpretable benchmarks are summarized in Table 2.

3.4.1. Random Forest (RF)

The Random Forest serves as a non-parametric ensemble baseline. It approximates the classification function $f(z)$ through an ensemble of $B = 100$ randomized decision trees. Each tree T_b partitions the redshift space into disjoint regions by identifying optimal split points s that minimize the Gini impurity:

$$G = 1 - \sum_{k=1}^K p_k^2, \quad (18)$$

where p_k denotes the fraction of samples belonging to class k within a given node. The final classification is determined via majority voting:

$$\hat{C}_{\text{RF}}(z) = \text{mode}\{T_1(z), T_2(z), \dots, T_B(z)\} \quad (19)$$

To prevent structural over-complexity, the trees are constrained to a maximum depth of 10, allowing the ensemble to model high-frequency population transitions while maintaining stability.

3.4.2. Support Vector Machine (SVM)

The SVM evaluates the separability of the manifold by projecting the one-dimensional input into a high-dimensional Hilbert space using a Radial Basis Function (RBF) kernel:

$$K(z, z') = \exp(-\gamma \|z - z'\|^2) \quad (20)$$

The classifier identifies optimal separating hyperplanes by maximizing the margin between astrophysical classes. With regularization parameter $C = 1.0$ and an RBF kernel, the SVM constructs smooth, non-linear decision boundaries, serving as a benchmark for global margin maximization without explicit functional-form constraints.

3.4.3. Multi-Layer Perceptron (MLP)

The MLP represents the connectionist approach, where the mapping $z \rightarrow \text{Class}$ is learned through hidden layers. We implement a (32, 16) architecture, where each layer computes

$$h^{(l)} = \sigma(W^{(l)}h^{(l-1)} + b^{(l)}), \quad (21)$$

with $\sigma(x) = \max(0, x)$ denoting the ReLU activation function. This model quantifies the performance of a high-capacity neural network relying on thousands of learned parameters, contrasting with the compact symbolic nodes explored in this work.

Table 1: Comparison of Symbolic Regression Frameworks: Engine, Objective, Optimization, and Scientific Inductive Bias

Method	Engine	Objective & Optimization	Inductive Bias
P _Y SR	Island-model GP (Julia)	$\mathcal{L} = \frac{1}{n} \sum (y_i - s(z_i))^2 + \alpha C$; local L-BFGS constant refinement per expression.	Functional survival through migratory evolutionary competition across independent populations.
ESR	GPU exhaustive enumeration	$S_{MDL} = \mathcal{L}_{neg} + \frac{k}{2} \ln(n) + C \ln(N_{ops} + 1)$; L-BFGS with 30 multi-start initializations.	Occam’s Razor; prioritizes the simplest globally valid mathematical structure.
PhySO	LSTM + risk-seeking policy gradient	$J(\phi) = \mathbb{E}_{s \sim p_\phi} [R(s) R \geq P_{90}]$; integrated L-BFGS tuning during sampling.	Dimensional stability via neural guardrails preventing unphysical growth.
MvSR	View-decomposed genetic programming	$\mathcal{L}_{agg} = \max(\text{MSE}_{V_1}, \text{MSE}_{V_2}, \text{MSE}_{V_3})$; independent L-BFGS refinement per view.	Population stratification across distinct astrophysical regimes.

3.4.4. Stratified Holdout Generalization Protocol

To rigorously evaluate robustness, we implement a Stratified Holdout Protocol. Each model is trained on an 80% partition of a representative 10,000-sample subset ($\mathcal{D}_{\text{train}} = 8,000$) and subsequently evaluated on the remaining 20% unseen test partition ($\mathcal{D}_{\text{test}} = 2,000$).

This protocol isolates *generalization stability*, ensuring that reported performance reflects genuine capture of the astrophysical manifold rather than localized over-fitting. The final performance metrics are reported following an automated Grid-SearchCV protocol to optimize hyperparameters such as the regularization C for SVM and tree depth for RF—specifically for the one-dimensional redshift manifold.

3.5. Performance Metrics and Evaluation Criteria

The evaluation of the symbolic regression (SR) frameworks is conducted through a multi-tiered diagnostic process. Because these models are required to perform a classification task using a regressive search engine, we distinguish between Functional Fidelity (regression accuracy) and Classification Reliability (the success of the population separation).

3.5.1. Functional Discovery and Structural Constraints

During the initial symbolic search, the input spectroscopic redshift (z) is mapped to a target ordinal encoding. The following criteria govern this discovery phase:

Mean Squared Error (MSE):. The primary loss function used during structural evolution is the MSE, which penalizes the squared distance between the symbolic output and the target label:

$$MSE = \frac{1}{n} \sum_{i=1}^n (y_i - s(z_i))^2. \quad (22)$$

In this study, MSE ensures the topological preservation of the dataset. By using an ordinal scale, we force the symbolic engine to discover functions that naturally increase or decrease along the redshift manifold.

Structural Complexity (C):. In accordance with Occam’s Razor, we enforce a complexity constraint to prevent over-fitting. Complexity is defined as the total node count ($|T|$) of the expression tree:

$$C(T) = \sum (\text{operators} + \text{variables} + \text{constants}) \leq 10 \quad (23)$$

Restricting $C \leq 10$ ensures that the resulting equations remain human-readable and mathematically parsimonious.

3.5.2. Classification Reliability and Statistical Agreement

After a scoring function $s(z)$ is finalized, it is discretized using two optimized thresholds, t_1 and t_2 . To evaluate the success of this discretization, we employ metrics that are robust against class imbalance:

Cohen’s Kappa (κ):. Unlike raw accuracy, Cohen’s κ measures the agreement between the model and the true labels while correcting for chance (Cohen, 1960) and is defined as follows:

$$\kappa = \frac{p_o - p_e}{1 - p_e}, \quad (24)$$

where p_o is the observed accuracy and p_e is the probability of random agreement, calculated as:

$$p_e = \frac{1}{N^2} \sum_k n_{k1} n_{k2} \quad (25)$$

where n_{k1} and n_{k2} are the marginal totals for class k in the confusion matrix.

Macro-Averaged F1-Score:. The F1-score is the harmonic mean of precision and recall. We utilize the Macro-average to provide an unweighted mean of per-class performance:

$$F1_k = \frac{2 \cdot \text{Precision}_k \cdot \text{Recall}_k}{\text{Precision}_k + \text{Recall}_k} \quad (26)$$

The macro average ($F1_{\text{macro}}$) is defined as follows:

$$F1_{\text{macro}} = \frac{1}{K} \sum_{k=1}^K F1_k, \quad (27)$$

where $K = 3$ is the total number of astrophysical classes.

Table 2: Comparison of Machine Learning Baselines: Paradigm, Objective, Optimization, and Inductive Bias

Model	Paradigm	Objective & Optimization	Inductive Bias
Random Forest (RF)	Ensemble learning	Minimization of Gini impurity via recursive axis-aligned partitioning; greedy heuristic search for locally optimal split points.	Ensemble averaging; assumes that the consensus of decorrelated decision trees smooths decision boundaries along population density gradients.
Support Vector Machine (SVM)	Kernel-based margin maximization	Maximization of the geometric margin under soft constraints; convex quadratic programming with RBF kernel transformation.	Maximum-margin principle; favors globally smooth, high-separation decision boundaries in transformed feature space.
Multi-Layer Perceptron (MLP)	Feed-forward neural network	Cross-entropy loss minimization via stochastic gradient descent (backpropagation) across layered nonlinear transformations.	Distributed representation learning; assumes hierarchical nonlinear feature composition captures latent manifold structure.

Balanced Accuracy:. Calculated as the arithmetic mean of class-specific recall values, this metric provides an unbiased accuracy score:

$$\text{Balanced Acc.} = \frac{1}{K} \sum_{k=1}^K \frac{TP_k}{TP_k + FN_k}, \quad (28)$$

where TP and FN are True Positives and False Negatives, respectively.

3.5.3. Physical Failure Analysis

To provide a deeper astrophysical interpretation, we utilize diagnostic tools that map mathematical errors to physical redshift regions:

Binned Recall Profiles ($R(z)$):. By calculating recall within narrow redshift windows Δz , we identify ‘‘Physical Transition Zones.’’

$$R(z)_k = \frac{TP_k(z \in \Delta z)}{TP_k(z \in \Delta z) + FN_k(z \in \Delta z)} \quad (29)$$

This identifies where the spectral signatures of populations become indistinguishable to a 1D model.

Kappa Sensitivity Heatmaps:. We generate 2D grid visualizations of κ across a range of t_1 and t_2 . This evaluates the robustness of the decision manifold by verifying the stability of the global maximum:

$$\mathcal{S}_k(t_1, t_2) = \kappa(s(z), t_1, t_2) \quad (30)$$

3.6. Automated Threshold Optimization Protocol

To ensure that no framework is unfairly disadvantaged, we implement a Unified Optimization Protocol. For every scoring function $s(z)$, the decision boundaries are calibrated using a stratified grid-search on the validation set V :

Search Range:. t is constrained within the empirical percentiles of the validation scores:

$$t \in [P_5(s(V)), P_{95}(s(V))] \quad (31)$$

The protocol strictly enforces the ordering of the boundaries:

$$t_1 < t_2 \quad (32)$$

The threshold pair (t_1^*, t_2^*) is selected by maximizing the Cohen’s κ :

$$(t_1^*, t_2^*) = \arg \max_{t_1 < t_2} \kappa(s(V), y(V)) \quad (33)$$

4. Results and Analysis

We present a comprehensive evaluation of the symbolic regression (SR) frameworks, detailing the optimized analytic expressions, classification performance across the redshift manifold, and physical failure modes. As established in Section 3.2, all results are derived using 5-fold stratified cross-validation on 100,000 spectroscopically confirmed objects from SDSS DR17.

4.1. Framework-Specific Results

For each symbolic framework, we provide a diagnostic suite consisting of the discovered scoring function, average confusion matrices, threshold sensitivity analysis, and class-specific recall profiles.

4.1.1. P_{YSR} : Evolutionary Island-Model Discovery

Discovered Expression. The representative scoring function identified by P_{YSR} captures non-linear population transitions using linear redshift scaling and a sharp exponential decay:

$$s(z) = 0.8395 z + e^{-78.28z} - 0.1141 \quad (34)$$

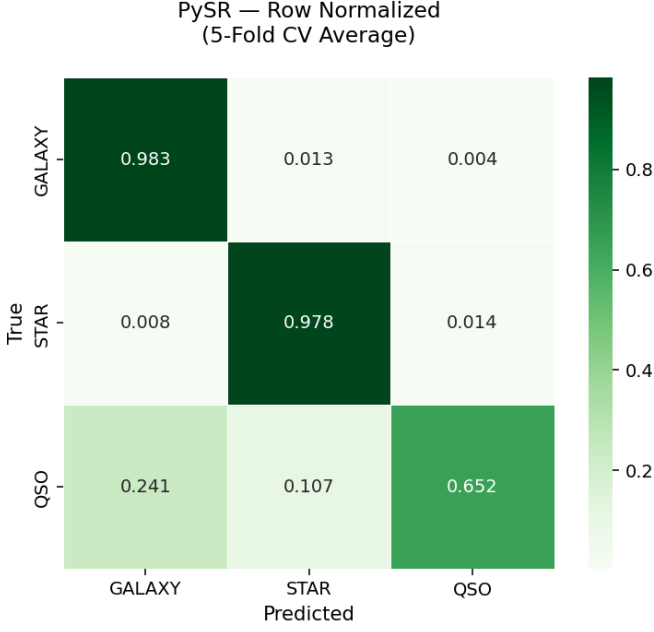


Figure 9: Average Row-Normalized Confusion Matrix — PySR (5-Fold CV). The heatmap shows the fraction of actual classes correctly predicted as GALAXY (0.983), STAR (0.978), and QSO (0.651).

Classification Performance and Stability. PySR achieves a mean Cohen’s κ of 0.8526 ± 0.0032 and an accuracy of $91.92 \pm 0.0017\%$. The average row-normalized confusion matrix, shown in Figure 9, demonstrates exceptional fidelity for GALAXY (0.983) and STAR (0.978) populations.

However, a non-negligible fraction of QSO samples (0.241) is misclassified as galaxies, reflecting spectral overlap in a one-dimensional redshift feature space. This results in a class-specific $F1_{\text{QSO}}$ of 0.7759 ± 0.0049 . The framework exhibits moderate variability in its decision boundaries, with a threshold standard deviation of $\sigma_{t_1} = 0.017$.

Error and Physical Failure Analysis. Analysis of the error distribution, visualized in Figure 10, pinpoints the physical boundaries where the analytic form reaches its limit.

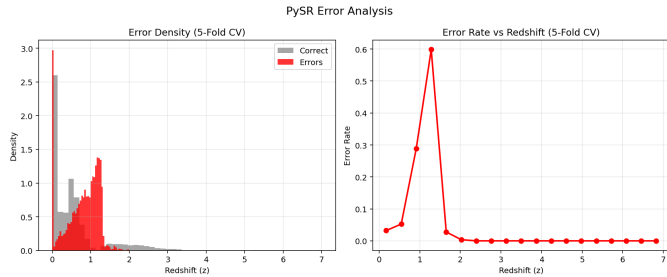


Figure 10: PySR Error Analysis. Left: Error density distribution showing correctly classified objects (gray) versus misclassifications (red) across redshift. Right: The Error rate vs. redshift profile, revealing a sharp failure spike peaking near $z \approx 1.25$.

Misclassifications are nearly absent at $z \approx 0$ (stellar locus) but become prominent between $z \approx 0.8$ and $z \approx 1.5$, where the

analytic form struggles to separate overlapping galaxy–QSO populations.

Threshold Robustness and Model Stability. The robustness of the discovered decision manifold is illustrated through the Kappa sensitivity landscape in Figure 11.

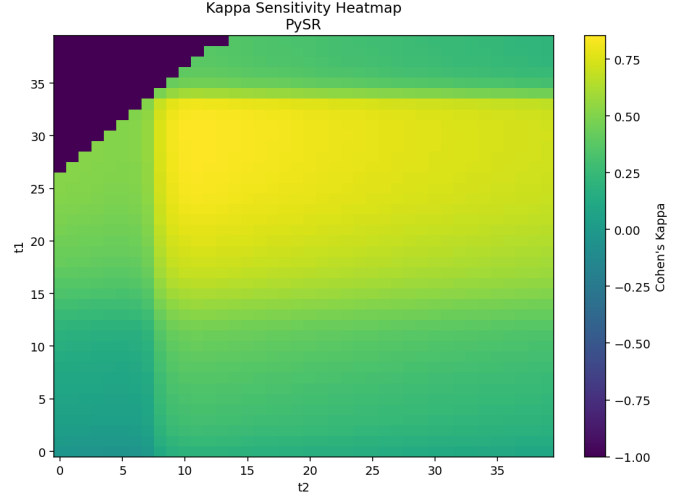


Figure 11: Kappa Sensitivity Heatmap — PySR . A 2D grid visualizing Cohen’s κ as a function of decision thresholds t_1 and t_2 . A broad high-value plateau indicates stable class separation.

A broad high-value plateau is visible across a wide range of t_1 and t_2 combinations, indicating that $s(z)$ is not overly sensitive to minor threshold perturbations. The optimized thresholds remain consistent across folds:

$$t_1 = 0.796 \pm 0.017, \quad t_2 = 0.981 \pm 0.011. \quad (35)$$

Recall Profiles and Physical Transition Dynamics. The Recall vs. Redshift profile (Figure 12) summarizes the physical transition behavior of the classifier.

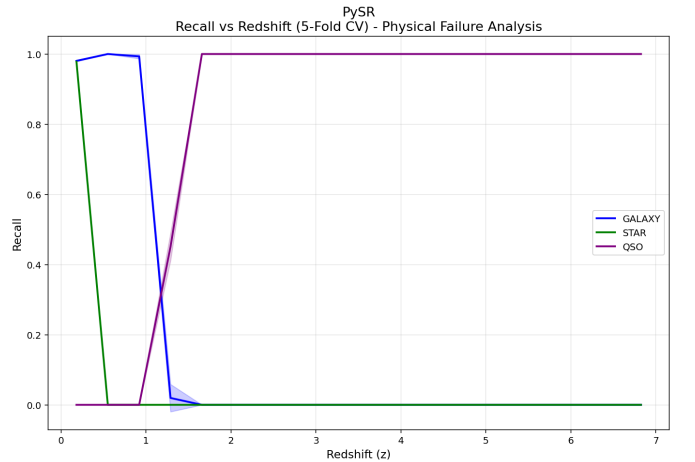


Figure 12: Recall vs. Redshift — Physical Failure Analysis (PySR). Class-wise recall across redshift with shaded regions representing the standard deviation over 5 folds.

STAR recall remains near unity for $z < 0.5$ before sharply declining as the GALAXY regime emerges. GALAXY recall stays near 1.0 until $z \approx 0.9$, after which it drops rapidly as QSO recall rises to unity. The narrow shaded region near $z \approx 1.5$ indicates minor fold-to-fold variability in modeling the crossover boundary.

4.1.2. ESR: Exhaustive MDL-Based Selection

Discovered Expression. The deterministic search provided by ESR favors a parsimonious quadratic form with a dampened exponential term, ensuring a structurally stable functional mapping:

$$s(z) = 0.7 + z^2 + e^{-11.88z} \quad (36)$$

Classification Performance and Stability. ESR demonstrates superior quasar identification relative to the evolutionary baseline, yielding a mean $F1_{\text{QSO}}$ of 0.8138 ± 0.0047 . The framework achieves a mean Cohen's κ of 0.8665 ± 0.0030 and an overall accuracy of $92.60 \pm 0.0017\%$.

The average row-normalized confusion matrix, shown in Figure 13, confirms robust performance across all classes, with particularly high fidelity for STAR (0.997) and GALAXY (0.974) populations.

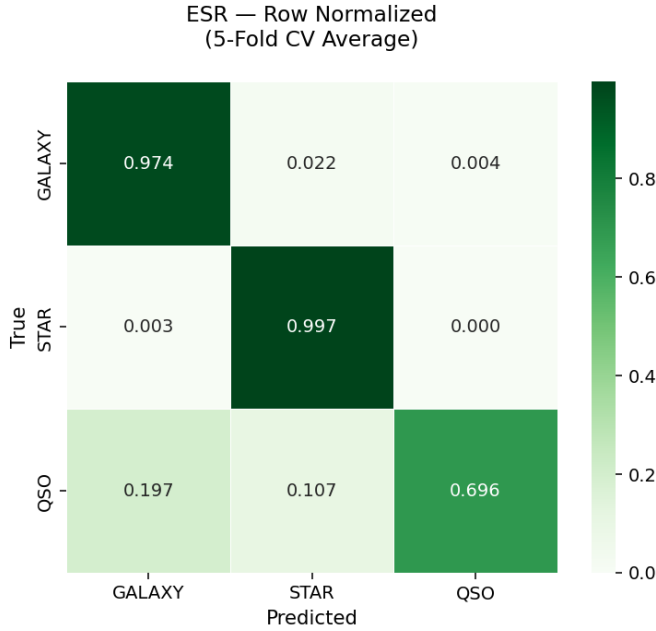


Figure 13: Average Row-Normalized Confusion Matrix — ESR (5-Fold CV). The heatmap shows the fraction of actual classes correctly predicted as GALAXY (0.974), STAR (0.997), and QSO (0.696).

The optimized decision thresholds remain consistent across all folds:

$$t_1 = 1.658 \pm 0.027, \quad t_2 = 2.193 \pm 0.023. \quad (37)$$

Error and Physical Failure Analysis. Analysis of the error distribution reveals that misclassifications are concentrated within the range $z \approx 0.8$ to $z \approx 1.5$.

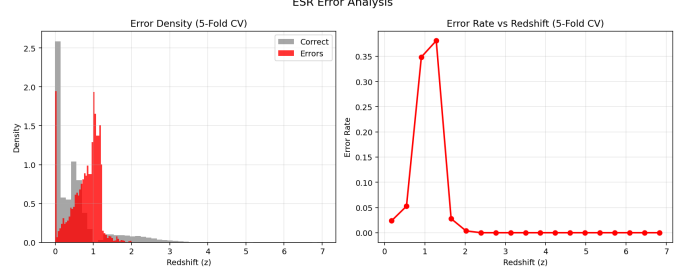


Figure 14: ESR Error Analysis. Left: Error density distribution showing correctly classified objects (gray) versus misclassifications (red) across redshift. Right: Error rate vs. redshift profile indicating a peak failure rate of approximately 0.38 near $z \approx 1.25$.

The Error Rate vs. Redshift profile (Figure 14) demonstrates a peak failure rate of approximately 0.38 near $z \approx 1.25$, significantly more suppressed than the spikes observed in heuristic search methods.

Threshold Robustness and Model Stability. The robustness of the MDL-selected decision manifold is illustrated through the Kappa sensitivity landscape in Figure 15.

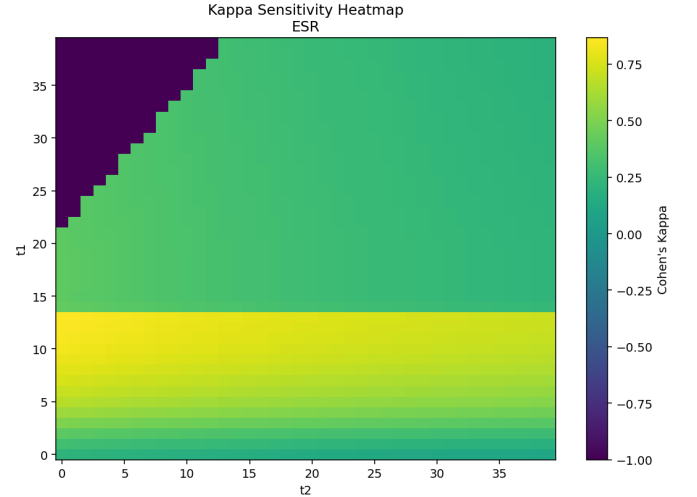


Figure 15: Kappa Sensitivity Heatmap — ESR. A 2D grid visualizing Cohen's κ as a function of decision thresholds t_1 and t_2 , highlighting an expansive optimal plateau.

The extensive high-value plateau indicates that the analytic form is less sensitive to minor threshold shifts, suggesting that the MDL-based selection successfully identifies a physically robust scoring manifold that generalizes well across different data samples.

Recall Profiles and Physical Transition Dynamics. The curve for recoil as a function of redshift (Figure 16) highlights the framework's reliable recovery of the stellar population ($z < 0.5$).

Similar to other models, a characteristic crossover exists between $z \approx 1.0$ and $z \approx 1.5$, where GALAXY recall falls as QSO recall rises, defining the physical boundary of one-dimensional redshift separation.

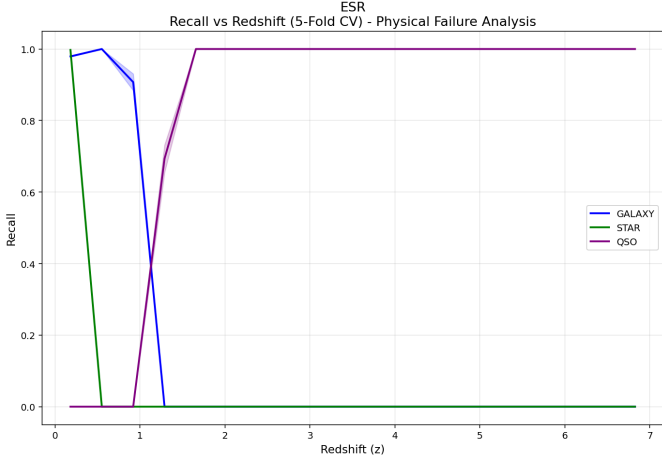


Figure 16: Recall vs. Redshift — Physical Failure Analysis (ESR). Line plot displaying recall for each class across the redshift range, with shaded regions denoting the standard deviation across 5 folds.

4.1.3. PhySO: Deep Reinforcement Learning Optimization

Discovered Expression. The reinforcement learning agent discovers a nested functional motif that precisely maps redshift transitions by identifying stable, Gaussian-like structures:

$$s(z) = 2.4027 - e^{0.5786 - z^2 + z} \quad (38)$$

Classification Performance and Stability. PhySO exhibits exceptional parametric stability, achieving the lowest threshold standard deviation in the study:

$$t_1 = 0.587 \pm 0.001, \quad t_2 = 0.908 \pm 0.002. \quad (39)$$

The framework yields a mean Cohen’s κ of 0.8749 ± 0.0018 and an overall accuracy of $93.05 \pm 0.0010\%$.

The average row-normalized confusion matrix, illustrated in Figure 17, demonstrates nearly perfect identification of the STAR population (1.000) and high fidelity for GALAXY (0.969), while maintaining a robust QSO identification rate of 0.730.

Error and Physical Failure Analysis. Analysis of the error distribution indicates that misclassifications are almost entirely absent at $z \approx 0$, but concentrate between $z \approx 0.8$ and $z \approx 1.5$.

The Error Rate vs. Redshift profile, visualized in Figure 18, reveals a suppressed peak failure rate of approximately 0.34 near $z \approx 1.0$, characterizing a smoother transition manifold than evolutionary baselines.

Threshold Robustness and Model Stability. The robustness of the discovered physical law is illustrated through the Kappa sensitivity landscape in Figure 19.

The broad optimal plateau indicates that the analytic form provided by PhySO is highly stable and resistant to minor fluctuations in threshold calibration, confirming its utility for automated spectroscopic pipelines.

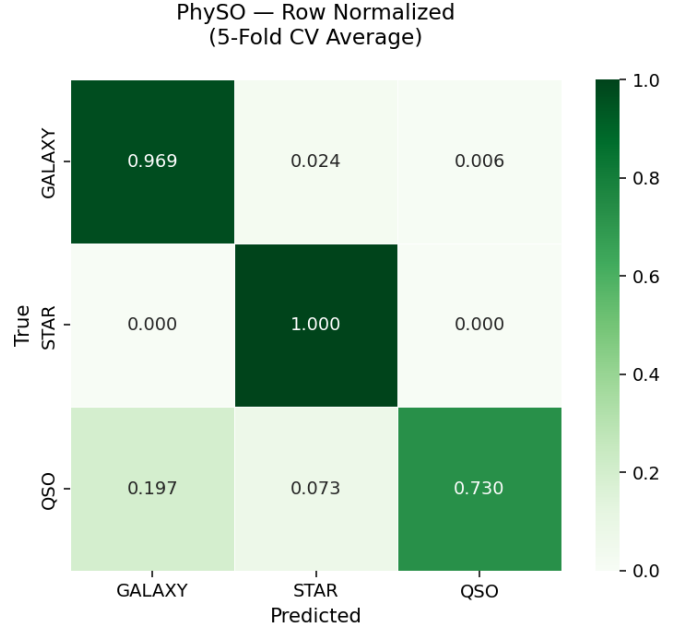


Figure 17: Average Row-Normalized Confusion Matrix — PhySO (5-Fold CV). The heatmap illustrates the fraction of actual classes correctly predicted, featuring perfect STAR identification (1.000) and high GALAXY (0.969) accuracy.

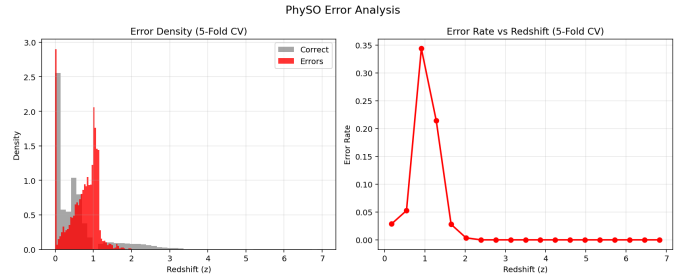


Figure 18: PhySO Error Analysis. Left: Error density distribution comparing correctly classified objects (gray) versus misclassifications (red) across redshift. Right: Error rate vs. redshift profile showing a peak error rate of approximately 0.34 near $z \approx 1.0$.

Recall Profiles and Physical Transition Dynamics. The Recall vs. Redshift profile (Figure 20) confirms that STAR recall is maintained at 1.0 until $z \approx 0.5$.

The GALAXY recall remains high until $z \approx 1.0$, dropping as the QSO recall rises to 1.0, with minimal variance observed across the crossover boundary.

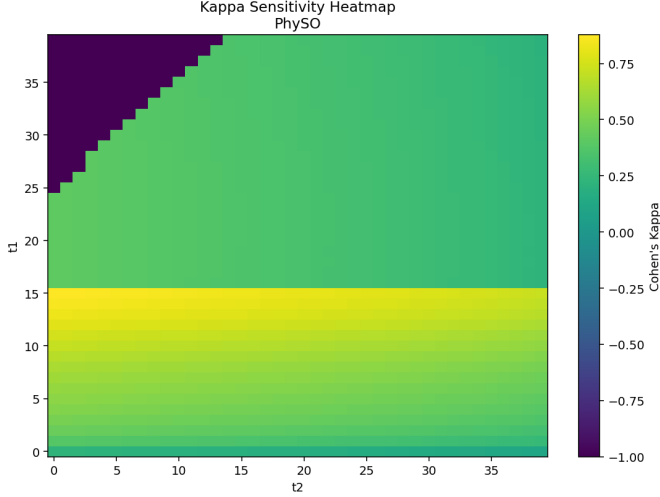


Figure 19: Kappa Sensitivity Heatmap — *PhySO*. A 2D grid visualizing Cohen's κ as a function of decision thresholds t_1 and t_2 , highlighting a stable and clearly defined optimal region.

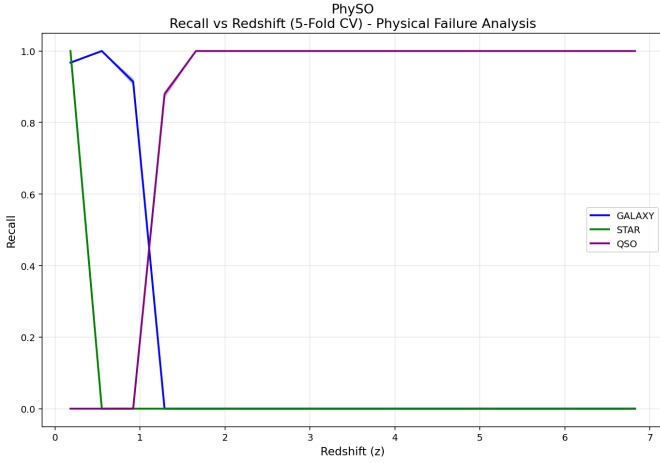


Figure 20: Recall vs. Redshift — Physical Failure Analysis (*PhySO*). Line plot showing recall for each class across the redshift range, indicating precise boundary separation between populations.

4.1.4. *MvSR*: Multi-View Specialist Evolution

Discovered Expression. *MvSR* discovers a globally shared template incorporating a physically motivated rational form to address non-stationarity across the redshift manifold:

$$s(z) = 3.134 - \frac{2.320}{z + e^{-2.904z}} \quad (40)$$

Classification Performance and Stability. *MvSR* emerges as the top-performing framework across all primary metrics (as summarized in Table 3), achieving a mean Cohen's κ of 0.8948 ± 0.0030 and an overall accuracy of $94.11 \pm 0.0017\%$.

The model demonstrates superior class-specific robustness, visualized in the confusion matrix in Figure 21, particularly for the STAR population ($F1 = 0.9745$) and the underrepresented QSO class ($F1 = 0.8618$).

Furthermore, *MvSR* maintains high decision boundary precision with minimal variance across folds:

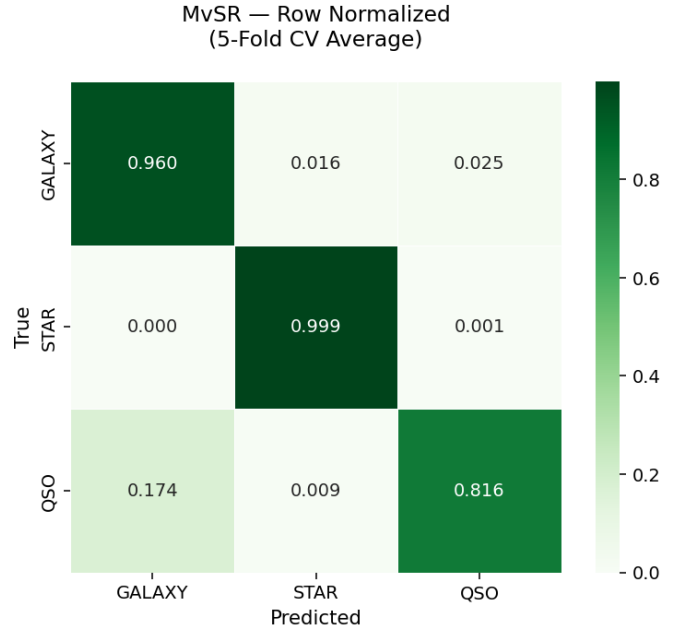


Figure 21: Average Row-Normalized Confusion Matrix — *MvSR* (5-Fold CV). The heatmap shows near-perfect identification of STAR (0.999) and GALAXY (0.960) populations, with significantly improved QSO (0.816) accuracy.

$$t_1 = 0.776 \pm 0.002, \quad t_2 = 0.830 \pm 0.003. \quad (41)$$

Error and Physical Failure Analysis. Analysis of the error distribution shows that *MvSR* effectively flattens the major error spikes observed in single-view methods.

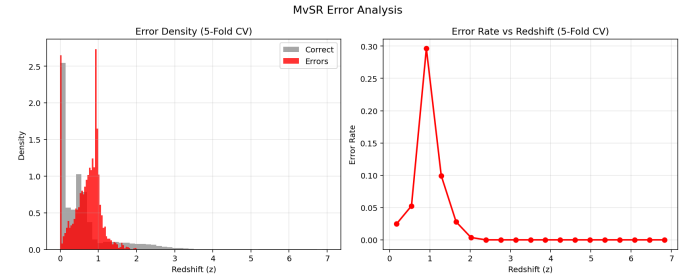


Figure 22: *MvSR* Error Analysis. Left: Error density distribution illustrating correctly classified objects (gray) relative to misclassifications (red). Right: Error rate vs. redshift profile showing a suppressed peak failure rate of approximately 0.30 near $z \approx 0.9$.

The plot for Error rate as a function of redshift (Figure 22) indicates a peak failure rate of approximately 0.30 near $z \approx 0.9$, significantly lower and shifted compared to the $z \approx 1.25$ spikes observed in *PySR* and *ESR*.

Threshold Robustness and Model Stability. The Kappa Sensitivity heatmap (Figure 23) reveals an expansive and uniform optimal plateau.

The broad high-value region indicates exceptional stability, suggesting that the discovered analytic form represents a robust physical mapping of the SDSS DR17 dataset and is highly resistant to minor threshold calibration errors.

Table 3: Comprehensive Performance Metrics and Threshold Stability for Symbolic Regression Frameworks

Method	Cohen's κ	Accuracy	Bal. Acc.	Macro-F1	$t_1 \pm \sigma$	$t_2 \pm \sigma$
PySR	0.8526 ± 0.0032	0.9192 ± 0.0017	0.8709 ± 0.0026	0.8856 ± 0.0025	0.796 ± 0.017	0.981 ± 0.011
ESR	0.8665 ± 0.0030	0.9260 ± 0.0017	0.8889 ± 0.0024	0.8988 ± 0.0028	1.658 ± 0.027	2.193 ± 0.023
PhySO	0.8749 ± 0.0018	0.9305 ± 0.0010	0.8997 ± 0.0014	0.9088 ± 0.0014	0.587 ± 0.001	0.908 ± 0.002
MvSR	0.8948 ± 0.0030	0.9411 ± 0.0017	0.9251 ± 0.0016	0.9296 ± 0.0020	0.776 ± 0.002	0.830 ± 0.003

Table 4: Performance Metrics for Optimized Machine Learning Baselines

Model	Paradigm	CV κ (Discovery Phase)	CV κ (Global Test Set)	Macro-F1
Random Forest	Ensemble (Tree-Based)	0.8953 ± 0.008	0.8937	0.9293
Support Vector Machine	Kernel-Based	0.8954 ± 0.009	0.9007	0.9335
Multi-Layer Perceptron	Neural Network	0.8934 ± 0.007	0.9028	0.9352

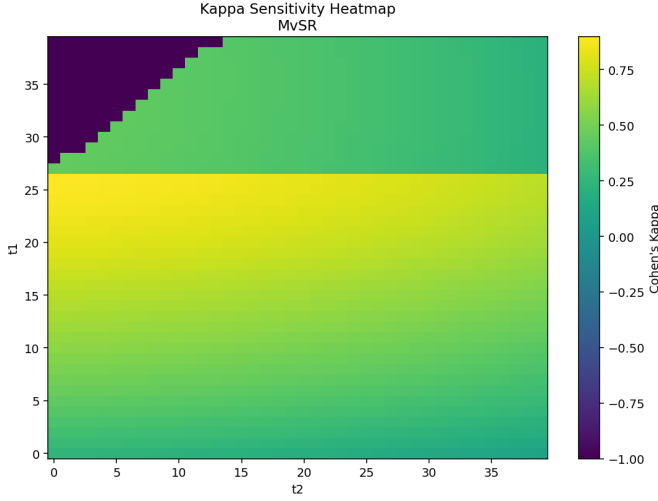


Figure 23: Kappa Sensitivity Heatmap — MvSR. A 2D grid visualizing Cohen's κ as a function of decision thresholds t_1 and t_2 , demonstrating the most expansive and stable optimal region in the study.

Recall Profiles and Physical Transition Dynamics. The Recall vs. Redshift profile (Figure 24) highlights MvSR's advanced population separation capability.

MvSR maintains a GALAXY recall of nearly 1.0 until $z \approx 1.0$, extending the reliable classification boundary further into the high-redshift regime before the transition to QSO dominance.

4.2. Performance Analysis of Optimized Machine Learning Baselines

The evaluation of non-interpretable benchmarks establishes the empirical performance ceiling for the classification task within the spectroscopic redshift manifold. By utilizing the optimized hyperparameters determined in the methodology, these models provide a rigorous comparative baseline to evaluate the representational efficiency of the symbolic expressions.

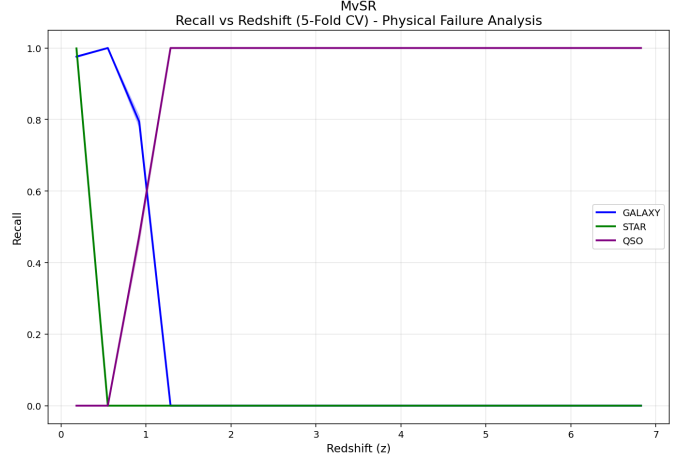


Figure 24: Recall vs. Redshift — Physical Failure Analysis (MvSR). Line plot showing recall for each class across the redshift range, illustrating the cleanest separation between galaxies and quasars across the redshift manifold.

4.2.1. Predictive Performance and Information-Theoretic Ceiling

The results of the five-fold stratified cross-validation demonstrate, as detailed in Table 4, a definitive convergence in predictive agreement across ensemble, connectionist, and kernel-based paradigms. The Support Vector Machine and Random Forest establish a consistent statistical ceiling, achieving mean CV κ values of 0.8954 ± 0.009 and 0.8953 ± 0.008 , respectively. The Multi-Layer Perceptron yielded the highest individual test performance with a κ of 0.9028.

The negligible improvement observed after exhaustive parameter tuning suggests that the predictive information inherent in the one-dimensional redshift feature space has been fully exhausted. This asymptotic behavior confirms that the remaining classification error is rooted in intrinsic physical degeneracies of the SDSS DR17 dataset rather than model architecture.

Table 5: Summary of Discovered Symbolic Expressions and Predictive Performance

Method	Discovered Expression $s(z)$	Cohen’s κ (mean \pm std)	Complexity
PySR	$0.8395z + e^{-78.28z} - 0.1141$	0.8526 ± 0.0032	10
ESR	$0.7 + z^2 + e^{-11.88z}$	0.8665 ± 0.0030	9
PhySO	$2.4027 - e^{0.5786-z^2+z}$	0.8749 ± 0.0018	10
MvSR	$3.134 - \frac{2.320}{z+e^{-2.904z}}$	0.8948 ± 0.0030	10

4.2.2. Class-Specific Sensitivity and Stability

The optimized baselines exhibit high stability across all primary metrics, with Macro-F1 scores remaining consistent near 0.93. The Support Vector Machine showed the most significant response to hyperparameter calibration, achieving a performance gain of $\Delta\kappa = +0.0176$ through optimal regularization.

The low standard deviation across folds ($\sigma < 0.01$) for all models reinforces the reliability of the 10,000-sample stratified subset as a representative proxy for the global astrophysical population. These results indicate that the decision boundaries learned by the black-box models are robust and well-defined along the population density gradients.

4.2.3. Comparison of Representational Complexity

The most critical insight from the baseline analysis is the absence of a substantial performance advantage for high-capacity models over the compact symbolic frameworks. Even with thousands of trainable parameters and non-linear transformations, the connectionist and ensemble models were unable to significantly surpass the $\kappa \approx 0.90$ barrier.

This justifies the use of symbolic regression as a parsimonious alternative; the ten-node analytic expressions discovered in previous sections achieve nearly identical performance to these optimized benchmarks while offering complete mathematical transparency.

5. Conclusions

This work presented a systematic comparative evaluation of four state-of-the-art symbolic regression frameworks and three optimized machine learning baselines for the classification of stars, galaxies, and quasars in the SDSS DR17 and extends the analysis in [Llorella and Cebrian \(2025\)](#). By restricting the feature space to spectroscopic redshift, we isolated the representational capacity of each paradigm to discover stable, non-linear decision manifolds.

5.1. Summary of Framework Performance

Our results demonstrate that symbolic regression can achieve predictive parity with high-capacity black-box models. The Multi-View Symbolic Regression (MvSR) framework emerged as the top-performing symbolic engine, achieving a Cohen’s κ of 0.8948 ± 0.0030 and a Balanced Accuracy of $92.51 \pm 0.0016\%$. This performance is statistically indistinguishable from the optimized Random Forest ($\kappa = 0.8953$) and Support Vector Machine

($\kappa = 0.8954$) baselines. A consolidated overview of these discovered expressions and their performance metrics is presented in [Table 5](#).

Furthermore, frameworks like PhySO demonstrated exceptional parametric stability, yielding threshold standard deviations ($\sigma < 0.002$) an order of magnitude lower than traditional evolutionary search methods.

5.2. The Information-Theoretic Limit

The convergence of all optimized models at a performance ceiling of $\kappa \approx 0.90$ indicates that the remaining classification error is rooted in intrinsic physical degeneracies of the SDSS DR17 redshift distribution. Specifically, the overlap in spectroscopic signatures between galaxies and quasars near $z \approx 1.25$ represents a fundamental Bayes error rate within a one-dimensional feature space.

The fact that compact, ten-node analytic expressions reach this same plateau suggests that the underlying astrophysical logic is governed by parsimonious geometric decision boundaries.

5.3. Scientific Impact and Future Work

The discovered analytic functions provide a transparent and computationally efficient alternative to traditional star–galaxy–quasar separation pipelines. Unlike neural networks or ensemble models, these human-readable expressions can be directly integrated into automated spectroscopic workflows without large-scale model persistence requirements.

Future research will explore the integration of photometric colors and multi-wavelength features into the symbolic discovery phase to resolve the high-redshift degeneracies identified in this study. Ultimately, this work reinforces the utility of symbolic regression as a framework for interpretable, physics-aware machine learning in the era of large-scale astronomical surveys.

6. ACKNOWLEDGEMENTS

We would like to thank the Sloan Digital Sky Survey (SDSS) and the Kaggle platform for sharing their data. R.D. acknowledges a postgraduate fellowship from the Ministry of Education (MoE), Government of India.

References

Abdurro’uf, Accetta, K., Aerts, C., Silva Aguirre, V., Ahumada, R., Ajaonkar, N., Filiz Ak, N., Alam, S., Allende Prieto, C.,

- Almeida, A., Anders, F., Anderson, S.F., Andrews, B.H., An-
guiano, B., Aquino-Ortíz, E., Aragón-Salamanca, A., Argudo-
Fernández, M., Ata, M., Aubert, M., Avila-Reese, V., Badenes,
C., Barbá, R.H., Barger, K., Barrera-Ballesteros, J.K., Beaton,
R.L., Beers, T.C., Belfiore, F., Bender, C.F., Bernardi, M., Ber-
shady, M.A., Beutler, F., Bidin, C.M., Bird, J.C., Bizyaev, D.,
Blanc, G.A., Blanton, M.R., Boardman, N.F., Bolton, A.S.,
Boquien, M., Borissova, J., Bovy, J., Brandt, W.N., Brown, J.,
Brownstein, J.R., Brusa, M., Buchner, J., Bundy, K., Burchett,
J.N., Bureau, M., Burgasser, A., Cabang, T.K., Campbell,
S., Cappellari, M., Carlberg, J.K., Wanderley, F.C., Carrera,
R., Cash, J., Chen, Y.P., Chen, W.H., Cherinka, B., Chiap-
pini, C., Choi, P.D., Chojnowski, S.D., Chung, H., Clerc,
N., Cohen, R.E., Comerford, J.M., Comparat, J., da Costa,
L., Covey, K., Crane, J.D., Cruz-Gonzalez, I., Culhane, C.,
Cunha, K., Dai, Y.S., Damke, G., Darling, J., Davidson, Jr.,
J.W., Davies, R., Dawson, K., De Lee, N., Diamond-Stanic,
A.M., Cano-Díaz, M., Sánchez, H.D., Donor, J., Duckworth,
C., Dwelly, T., Eisenstein, D.J., Elsworth, Y.P., Emsellem,
E., Eracleous, M., Escoffier, S., Fan, X., Farr, E., Feng, S.,
Fernández-Trincado, J.G., Feuillet, D., Filipp, A., Fillingham,
S.P., Frinchaboy, P.M., Fromenteau, S., Galbany, L., García,
R.A., García-Hernández, D.A., Ge, J., Geisler, D., Gelfand,
J., Géron, T., Gibson, B.J., Goddy, J., Godoy-Rivera, D.,
Grabowski, K., Green, P.J., Greener, M., Grier, C.J., Griffith,
E., Guo, H., Guy, J., Hadjara, M., Harding, P., Hasselquist, S.,
Hayes, C.R., Hearty, F., Hernández, J., Hill, L., Hogg, D.W.,
Holtzman, J.A., Horta, D., Hsieh, B.C., Hsu, C.H., Hsu, Y.H.,
Huber, D., Huertas-Company, M., Hutchinson, B., Hwang,
H.S., Ibarra-Medel, H.J., Chitham, J.I., Ilha, G.S., Imig, J.,
Jaekle, W., Jayasinghe, T., Ji, X., Johnson, J.A., Jones, A.,
Jönsson, H., Katkov, I., Khalatyan, Dr., A., Kinemuchi, K.,
Kisku, S., Knapen, J.H., Kneib, J.P., Kollmeier, J.A., Kong,
M., Kounkel, M., Kreckel, K., Krishnarao, D., Lacerna, I.,
Lane, R.R., Langgins, R., Lavender, R., Law, D.R., Lazarz, D.,
Leung, H.W., Leung, H.H., Lewis, H.M., Li, C., Li, R., Lian,
J., Liang, F.H., Lin, L., Lin, Y.T., Lin, S., Lintott, C., Long,
D., Longa-Peña, P., López-Cobá, C., Lu, S., Lundgren, B.F.,
Luo, Y., Mackereth, J.T., de la Macorra, A., Mahadevan, S.,
Majewski, S.R., Machado, A., Mandeville, T., Maraston, C.,
Margalef-Bentabol, B., Masseron, T., Masters, K.L., Mathur,
S., McDermid, R.M., McKay, M., Merloni, A., Merrifield, M.,
Meszaros, S., Miglio, A., Di Mille, F., Minniti, D., Minsley,
R., Monachesi, A., 2022. The Seventeenth Data Release of
the Sloan Digital Sky Surveys: Complete Release of MaNGA,
MaStar, and APOGEE-2 Data. *ApJS* 259, 35. [2112.02026](#).
- Bartlett, D.J., Desmond, H., Ferreira, P.G., 2022. Ex-
haustive Symbolic Regression. *arXiv e-prints* ,
[arXiv:2211.114612211.11461](#).
- Bartlett, D.J., Desmond, H., Ferreira, P.G., Kronberger, G., 2025.
Introduction to Symbolic Regression in the Physical Sciences.
arXiv e-prints , [arXiv:2512.159202512.15920](#).
- Bethapudi, S., Desai, S., 2018. Separation of pulsar signals
from noise using supervised machine learning algorithms.
Astronomy and Computing 23, 15. [1704.04659](#).
- Bhavanam, S.R., Channappayya, S.S., P. K, S., Desai, S., 2024.
Enhanced astronomical source classification with integration
of attention mechanisms and vision transformers. *Ap&SS*
369, 92. [2408.13634](#).
- Bishop, C.M., 2006. *Pattern Recognition and Machine Learning*.
Springer, New York.
- Chaini, S., Bagul, A., Deshpande, A., Gondkar, R., Sharma, K.,
Vivek, M., Kembhavi, A., 2023. Photometric identification
of compact galaxies, stars, and quasars using multiple neural
networks. *MNRAS* 518, 3123–3136. [2211.08388](#).
- Cohen, J., 1960. A coefficient of agreement for nominal scales.
Educational and psychological measurement 20, 37–46.
- Cranmer, M., 2023. Interpretable Machine Learning for Sci-
ence with PySR and SymbolicRegression.jl. *arXiv e-prints* ,
[arXiv:2305.015822305.01582](#).
- Darc, P., Bom, C.R., Kilpatrick, C., Fraga, B.M.O., Teixeira,
G.S.M., 2025. Symbolic Regression Is All You Need: From
Simulations to Scaling Laws in Binary Neutron Star Mergers.
arXiv e-prints , [arXiv:2511.087842511.08784](#).
- Desai, S., Armstrong, R., Mohr, J.J., Semler, D.R., Liu, J.,
Bertin, E., Allam, S.S., Barkhouse, W.A., Bazin, G., Buckley-
Geer, E.J., Cooper, M.C., Hansen, S.M., High, F.W., Lin,
H., Lin, Y.T., Ngeow, C.C., Rest, A., Song, J., Tucker, D.,
Zenteno, A., 2012. The Blanco Cosmology Survey: Data
Acquisition, Processing, Calibration, Quality Diagnostics,
and Data Release. *ApJ* 757, 83. [1204.1210](#).
- Desmond, H., 2025. (Exhaustive) Symbolic Regression and
model selection by minimum description length. *arXiv e-
prints* , [arXiv:2507.130332507.13033](#).
- Hassija, V., Chamola, V., Mahapatra, A., Singal, A., Goel, D.,
Huang, K., Scardapane, S., Spinelli, I., Mahmud, M., Hus-
sain, A., 2024. Interpreting black-box models: a review on
explainable artificial intelligence. *Cognitive Computation* 16,
45–74.
- Krishak, A., Desai, S., 2020. Model comparison tests of mod-
ified gravity from the Eöt-Wash experiment. *J. Cosmology
Astropart. Phys.* 2020, 006. [2003.10127](#).
- Liu, D.C., Nocedal, J., 1989. On the limited memory bfgs
method for large scale optimization. *Mathematical program-
ing* 45, 503–528.
- Llorella, F.R., Cebrian, J.A., 2025. Exploring Symbolic Re-
gression and Genetic Algorithms for Astronomical Object
Classification. *The Open Journal of Astrophysics* 8, 27.
[2503.09220](#).
- Logan, C.H.A., Fotopoulou, S., 2020. Unsupervised star, galaxy,
QSO classification. Application of HDBSCAN. *A&A* 633,
A154. [1911.05107](#).

- Martín, A., Yasin, T., Bartlett, D.J., Desmond, H., Ferreira, P.G., 2026. Symbolically regressing dark matter halo profiles using weak lensing. arXiv e-prints , arXiv:2601.05203 [2601.05203](#).
- Patra, N.K., Malik, T., Zhou, K., Providência, C., 2026. Learning the relations between neutron star and nuclear matter properties with symbolic regression [2601.07727](#).
- Richards, G.T., Fan, X., Newberg, H.J., Strauss, M.A., Vanden Berk, D.E., Schneider, D.P., Yanny, B., Boucher, A., Burles, S., Frieman, J.A., Gunn, J.E., Hall, P.B., Ivezić, Ž., Kent, S., Loveday, J., Lupton, R.H., Rockosi, C.M., Schlegel, D.J., Stoughton, C., SubbaRao, M., York, D.G., 2002. Spectroscopic Target Selection in the Sloan Digital Sky Survey: The Quasar Sample. *AJ* 123, 2945–2975. [astro-ph/0202251](#).
- Russeau, E., Olivetti de França, F., Malanchev, K., Burlacu, B., Ishida, E.E.O., Leroux, M., Michelin, C., Moinard, G., Gangler, E., 2024. Multi-View Symbolic Regression. arXiv e-prints , arXiv:2402.04298 [2402.04298](#).
- Sevilla-Noarbe, I., Hoyle, B., Marchã, M.J., Soumagnac, M.T., Bechtol, K., Drlica-Wagner, A., Abdalla, F., Aleksić, J., Avestruz, C., Balbinot, E., Banerji, M., Bertin, E., Bonnett, C., Brunner, R., Carrasco-Kind, M., Choi, A., Giannantonio, T., Kim, E., Lahav, O., Moraes, B., Nord, B., Ross, A.J., Rykoff, E.S., Santiago, B., Sheldon, E., Wei, K., Wester, W., Yanny, B., Abbott, T., Allam, S., Brooks, D., Carnero-Rosell, A., Carretero, J., Cunha, C., da Costa, L., Davis, C., de Vicente, J., Desai, S., Doel, P., Fernandez, E., Flaugher, B., Frieman, J., Garcia-Bellido, J., Gaztanaga, E., Gruen, D., Gruendl, R., Gschwend, J., Gutierrez, G., Hollowood, D.L., Honscheid, K., James, D., Jeltema, T., Kirk, D., Krause, E., Kuehn, K., Li, T.S., Lima, M., Maia, M.A.G., March, M., McMahon, R.G., Menanteau, F., Miquel, R., Ogando, R.L.C., Plazas, A.A., Sanchez, E., Scarpine, V., Schindler, R., Schubnell, M., Smith, M., Smith, R.C., Soares-Santos, M., Sobreira, F., Suchyta, E., Swanson, M.E.C., Tarle, G., Thomas, D., Tucker, D.L., Walker, A.R., DES Collaboration, 2018. Star-galaxy classification in the Dark Energy Survey Y1 data set. *MNRAS* 481, 5451–5469. [1805.02427](#).
- Slater, C.T., Ivezić, Z., Lupton, R.H., 2020. Morphological Star-Galaxy Separation. *AJ* 159, 65. [1912.08210](#).
- Solorio-Ramírez, J.L., Jiménez-Cruz, R., Villuendas-Rey, Y., Yáñez-Márquez, C., 2023. Random forest algorithm for the classification of spectral data of astronomical objects. *Algorithms* 16, 293.
- Soumagnac, M.T., Abdalla, F.B., Lahav, O., Kirk, D., Sevilla, I., Bertin, E., Rowe, B.T.P., Annis, J., Busha, M.T., Da Costa, L.N., Frieman, J.A., Gaztanaga, E., Jarvis, M., Lin, H., Percival, W.J., Santiago, B.X., Sabiu, C.G., Wechsler, R.H., Wolz, L., Yanny, B., 2015. Star/galaxy separation at faint magnitudes: application to a simulated Dark Energy Survey. *MNRAS* 450, 666–680. [1306.5236](#).
- Sousa-Neto, A., Bengaly, C., Gonzalez, J.E., Alcaniz, J., 2025. Evidence for dynamical dark energy from DESI-DR2 and SN data? A symbolic regression analysis. arXiv e-prints , arXiv:2502.10506 [2502.10506](#).
- Tenachi, W., Ibata, R., Diakogiannis, F.I., 2023. Deep Symbolic Regression for Physics Guided by Units Constraints: Toward the Automated Discovery of Physical Laws. *ApJ* 959, 99. [2303.03192](#).